RESEARCH ARTICLE

WILEY

Micromechanical modeling for rate-dependent behavior of salt rock under cyclic loading

Xianda Shen[1,2] | Jihui Ding[3,4] | Chloé Arson[2] | Judith S. Chester[4] | Frederick M. Chester[4]

[1]Department of Civil and Environmental Engineering, Northwestern University, Evanston, IL, U.S.A

[2]School of Civil and Environmental Engineering, Georgia Institute of Technology, Atlanta, GA, U.S.A

[3]Department of Geophysics, Stanford University, Stanford, CA, U.S.A

[4]Department of Geology and Geophysics, Texas A&M University, College Station, TX, U.S.A

Correspondence
Xianda Shen, Department of Civil and Environmental Engineering, Northwestern University, Evanston, IL, U.S.A.
Email: xianda.shen@northwestern.edu

Present Address
Xianda Shen, 2145 Sheridan Road, Evanston

Summary

The dependence of rock behavior on the deformation rate is still not well understood. In salt rock, the fundamental mechanisms that drive the accumulation of irreversible deformation, the reduction of stiffness, and the development of hysteresis during cyclic loading are usually attributed to intracrystalline plasticity and diffusion. We hypothesize that at low pressure and low temperature, the rate-dependent behavior of salt rock is governed by water-assisted diffusion along grain boundaries. Accordingly, a chemo-mechanical homogenization framework is proposed in which the representative elementary volume (REV) is viewed as a homogeneous polycrystalline matrix that contains sliding grain-boundary cracks. The slip is related to the mass of salt ions that diffuse along the crack surface. The relationship between fluid inclusion-scale and REV-scale stresses and strains is established by using the Mori–Tanaka homogenization scheme. It is noted from the model that a lower strain rate and a larger number of sliding cracks enhance stiffness reduction and hysteresis. Thinner sliding cracks (i.e., thinner brine films) promote stiffness reduction and accelerate stress redistributions. The larger the volume fraction of the crack inclusions, the larger the REV deformation and the larger the hysteresis. Results presented in this study shed light on the mechanical behavior of salt rock that is pertinent to the design of geological storage facilities that undergo cyclic unloading, which could help optimize the energy production cycle with low carbon emissions.

KEYWORDS
homogenization, hysteresis, pressure solution, rate-dependent, salt rock, sliding mechanism

1 | INTRODUCTION

Salt rock is a favorable host material for geological storage of hydrocarbons, compressed-air energy storage (CAES), sequestration of CO_2, and disposal of radioactive waste because of its low permeability and ideal creep properties. Salt rock is made of bonded halite crystals. Crystal plasticity influences the development of microscopic cracks,[1,2] and intergranular sliding leads to the degradation of the elastic moduli of the polycrystal.[3-6] In salt rock, frictional sliding at grain boundaries is the primary accommodation mechanism at room temperature and in dry conditions, low confining pressure, and high strain rate.[7] Deformation is controlled by the normal and shear stresses at grain boundaries and by

the distribution of boundary orientations. The rate of diffusional sliding depends on the availability of water and on the shape of the grain boundaries.[8]

The strain rate is a significant factor in the mechanical behavior of salt rock.[10-12] At low strain rate, the dominant mechanism can be diffusion. At higher temperature solid state, diffusion can occur within the lattice of crystals (a phenomenon called Nabarro–Herring creep) or along the grain boundaries (a phenomenon called Coble creep).[13,14] The presence of intergranular brine can activate pressure solution at lower temperature.[15-19] Pressure solution in crystalline media involves dissolution at the grain-to-grain contacts that are under high stress, transportation of ions by diffusion in fluid films along grain boundaries, and re-precipitation at grain-to-grain contacts that are under low stress. In wet salt rock, pressure solution can dominate creep for temperatures below 350°C (Figure 1). The goal of this study is to gain a fundamental understanding of the mechanisms that influence the accumulation of irreversible deformation under cyclic loading and the development of hysteresis at low temperature and high strain rate.

The mechanical behavior of a polycrystalline rock can be described via homogenization of diverse and realistic microstructures, that is, by upscaling crystal-, boundary-, or grain- scale mechanisms to the scale of the volume of a specimen. The smallest material volume element above which an effective property does not vary with position of that element is called the representative elementary volume (REV).[20] Homogenization is a procedure that allows relating field variables at the microscale to those at the macroscale of the REV[21] and calculating the effective mechanical properties of a composite.

The REV is often viewed as a homogeneous matrix that contains several families of inclusions. The solution of the inclusion–matrix interaction problem was established by Eshelby[22] for an infinitely extended linear elastic matrix that contains ellipsoidal inclusions. Numerous models were since then developed to predict the effective properties of an inhomogeneous continuum with ellipsoidal inclusions based on Eshelby's solution.[23-25] The local strain (or stress) field is written as the sum of the far field strain (or stress) boundary condition plus a so-called disturbance strain (or stress) field (note that the reasoning is the same for mixed boundary conditions). In Eshelby's theory, the key idea is to model each inclusion by a domain that has the same stiffness as that of the matrix but to add a so-called eigenstrain (or eigenstress) field to the local strain (or stress) field in the inclusion. For instance, in the Mori–Tanaka scheme, the average disturbance strain (or stress) field in the matrix is zero, so that the average matrix strain (or stress) is equal to the far field strain. Physically, that means that inclusions interact with a matrix subjected to a uniform strain (or stress) in the far field.[26-28] The Mori–Tanaka scheme has been widely used because of its accuracy and simplicity,[29,30] for instance, to predict the deformation of voids and the propagation of cracks in porous media.[31] Each family of voids is regarded as a set of inclusions subjected to a pore pressure field that is independent from the stress field of the matrix. Pore pressure adds to the eigenstress that stems from the difference of stiffness between the matrix and the inclusions. The Mori–Tanaka scheme was also used to calculate the thermal expansion of composites. In this case, the eigenstrain is the thermal deformation, expressed as a function of the difference between the thermal expansion coefficient of the matrix and that of the inclusions.[32] It was noted that for a composite material that contains inclusions with eigenstrains other than the eigenstrains that stem from mechanical heterogeneity, the REV stiffness tensor predicted with the Mori–Tanaka scheme may violate symmetry requirements if inclusions have different orientations and shapes.[27,33]

In this paper, we propose a homogenization scheme to understand the rate dependent decrease of stiffness and the hysteretic behavior of salt rock documented during cyclic compression tests. The experimental procedures and results are presented in Section 2. On the basis of our experimental observations, we hypothesize that the rate-dependent
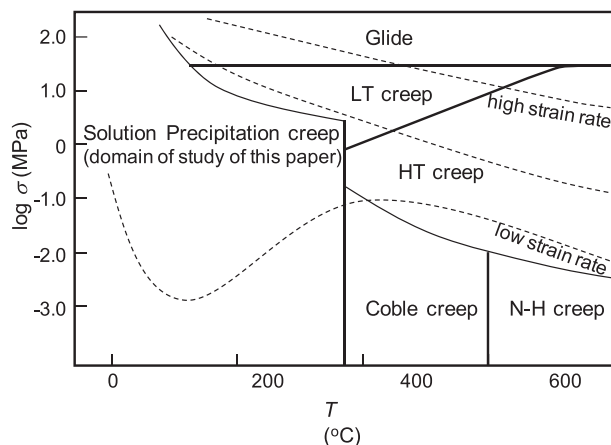

FIGURE 1 Deformation map of damp halite. LT represents low temperature; HT represents high temperature; N-H represents Nabarro–Hering[9]

behavior of salt rock is governed by pressure solution on grain boundaries. Accordingly, Section 3 explains grain boundary sliding by a micromechanical model based on the pressure-solution theory. In Section 4, a Mori–Tanaka homogenization scheme is used to upscale the local sliding mechanisms at the REV scale. In Section 5, the model is calibrated against the experimental results obtained for sets of loading cycles with permanent strain 0% and 3.8%. In Section 6, sensitivity analyses are conducted to evaluate the effects of local diffusion at grain contacts on the macroscopic deformation of salt rock. We discuss the mechanisms that most contribute to the dissipation of energy at REV scale in Section 7, and Section 8 summarizes the conclusions of this study.

2 | EXPERIMENTAL OBSERVATIONS DURING CYCLIC COMPRESSION TESTS

We conducted cyclic triaxial compression experiments on synthetic salt rock to study the viscoelastic behavior of salt aggregates.[34] Synthetic salt-rock specimens were fabricated by consolidating reagent-grade granular salt (grain diameter 0.3–0.355 mm) in a hollow cylindrical steel vessel under a maximum axial stress of 75 MPa, a temperature of 150°C, and a displacement rate of 0.34 mm/s. The consolidation took approximately 15 min. Fabricated specimens were right-circular cylinders (19-mm diameter and 43-mm length) with a bulk porosity of 5.45 ± 0.06%. Fabricated salt-rock specimens were installed in a triaxial vessel and loaded up to yield at a confining pressure of 1 MPa, at a strain rate of 3×10^{-5}/s, at room temperature, and in the absence of pore fluid. To characterize viscoelastic deformation as a function of inelastic strain, the specimens were then subjected to multiple loading cycles. In these conditions, specimen deformation involves a mixed-mode of grain boundary opening, sliding, and intracrystalline plasticity that manifests through viscoelastic behavior.[34]

In the cyclic triaxial compression tests, two types of loading cycles were utilized to characterize viscoelastic behavior: (1) a large loading cycle in which differential stress was cycled between zero-stress and the flow strength (∼40 MPa) and in which the specimen was deformed permanently by a specified increment of axial strain before the unloading portion of the cycle and (2) small loading cycles in which differential stress was cycled between 0 and 6.5 MPa and in which the specimen deformed elastically (Figure 2). Small loading cycles were implemented within large loading cycles at three different strain rates to quantify rate-dependent elastic behavior at a given axial strain. The first small loading cycle (C1) was applied at a rate of 3×10^{-5}/s, the second small loading cycle (C2) was applied at a rate of 3×10^{-6}/s, and the third small loading cycle (C3) was applied at a rate of 3×10^{-7}/s. The time period between C1 and C2 was 147 s, and the time period between C2 and C3 was 538 s. The unloading phases of small cycles were extended to allow slight separation of sample from the piston and therefore confirming full removal of axial load. Upon reloading, the axial load started increasing once the piston came into contact with the sample again. This resulted in a short period of zero load between small cycles, which increased in duration with decreasing reloading rate. Since the maximum differential stress in the small loading cycles was much lower than the yield stress of salt rock (see Figure 2), we considered that cracks did not propagate during the small loading cycles, and therefore, that damage accumulated during the large loading cycles only.

During the first set of small loading cycles, the stress–strain curves of C1, C2, and C3 exhibit the same linear elastic behavior (see Figures 2 and 3). The strain rate does not affect the stiffness of the specimen, and no significant hysteresis is observed. By contrast, the stress–strain curves obtained during the set of small cycles that followed the last large loading cycle after a permanent axial strain of 3.8% has been reached and exhibit a marked decrease of stiffness and
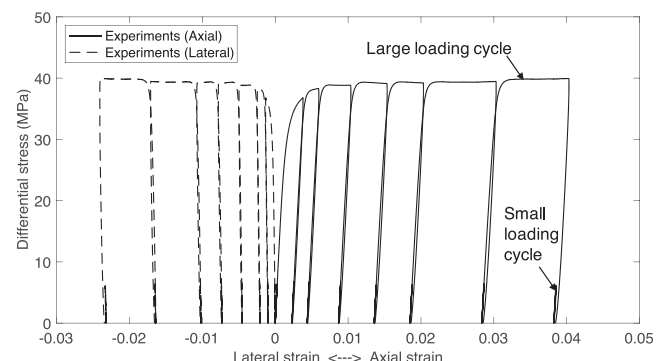

FIGURE 2 Stress–strain curve obtained during cyclic compression tests under a 1-MPa confining pressure. The maximum differential stress during large loading cycles is 40 MPa and about 6 MPa during small loading *cycles*[34,35]
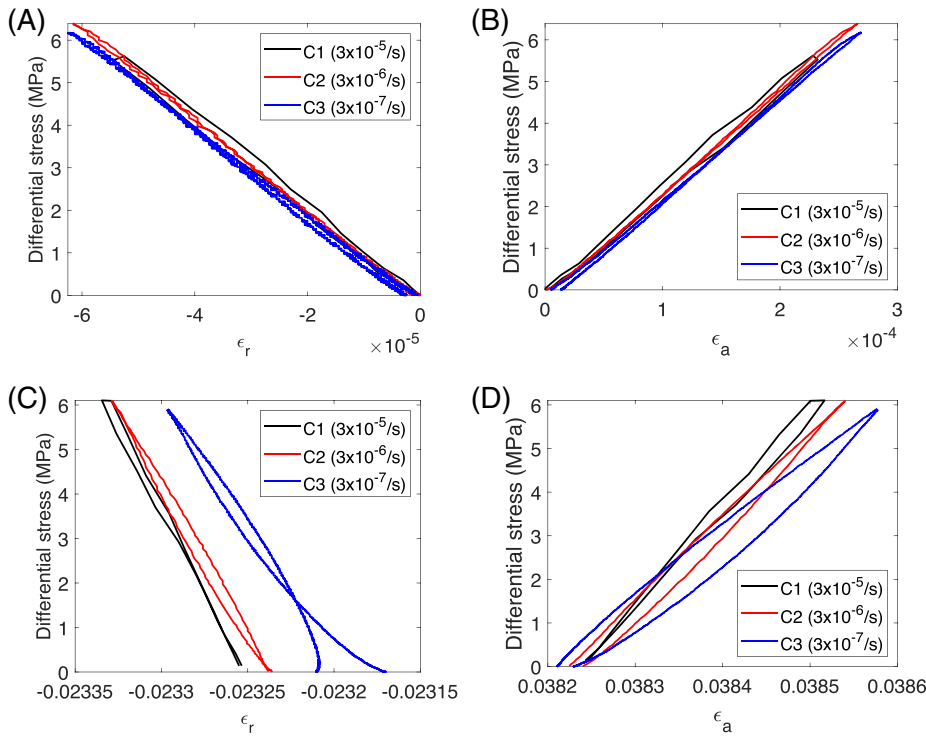
FIGURE 3 Plots of differential stress versus axial and radial strain obtained experimentally for the first and last set of small loading cycles. (A) C1–C3 radial stress–strain curve with ermanent axial strain $\epsilon_a = 0\%$. (B) C1–C3 axial stress–strain curve with permanent axial strain $\epsilon_a = 0\%$. (C) C1–C3 radial stress–strain curve with permanent axial strain $\epsilon_a = 3.8\%$. (D) C1–C3 axial stress–strain curve with permanent axial strain $\epsilon_a = 3.8\%$. ϵ_a is the axial strain. ϵ_r is the radial strain. The stress–strain relationship is linear when ϵ_a is 0%. When ϵ_a equals 3.8%, hysteresis occurs in the specimen, especially under lower strain rate[34] [Colour figure can be viewed at wileyonlinelibrary.com]

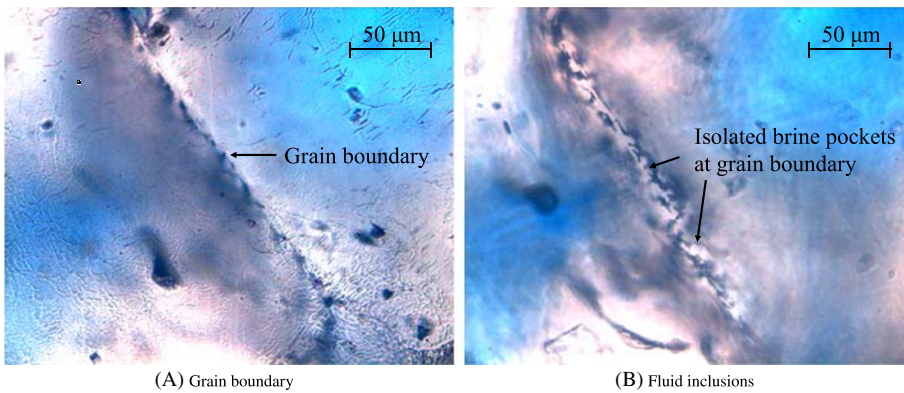(A) Grain boundary (B) Fluid inclusions

FIGURE 4 Isolated fluid inclusions along grain boundaries in undeformed consolidated sample (5% porosity)[34] [Colour figure can be viewed at wileyonlinelibrary.com]

pronounced hysteresis (see Figure 3C,D). Stiffness degradation and hysteresis are enhanced by low strain rate (i.e., stiffness degradation and hysteresis are more pronounced during C3 than C2 and more so in C2 than C1).

According to microscopic images taken after each large loading cycle (Figure 4), isolated fluid inclusions exist along the grain boundaries at the beginning of the cyclic compression test. After a few cycles, these fluid inclusions tend to connect to one another because of grain boundary sliding. A thin film forms at grain contacts. We hypothesize that this brine film facilitates diffusion along grain boundaries and enhances pressure solution at the grain contacts. In the following, we propose a micro–macro model to test this assumption. We simulate the behavior of salt rock during the small loading cycles, and we check that the model can be used to predict the rate dependence of the REV response.

3 | MICROMECHANCIAL MODEL OF GRAIN BOUNDARY SLIDING BY PRESSURE SOLUTION

3.1 | Conceptual model

From the discussion in Section 1 and the observations made in Section 2, we hypothesize that the rate-dependent behavior of salt rock is governed by pressure solution on grain boundaries at low pressure and low temperature. When subjected to normal stress, larger normal stress induces a higher chemical potential and the dissolution of salt crystals

at contacts. Ions diffuse along fluid films at crystal boundaries and precipitate at the contacts with less normal stress. Dissolution, diffusion, and precipitation happen simultaneously (but at different locations). Pressure solution thus happens due to the presence of brine films along contacting grain boundaries. We represent the REV as a solid salt matrix that contains intergranular shear-mode cracks. We model the shear-mode crack inclusions as a spherical volume containing a crack, referred as a crack inclusion. Within one crack inclusion, the sliding plane is characterized by its orientation in reference to the horizontal (angle θ), so that the REV is viewed as a distribution of oriented spherical volumes (crack inclusions) embedded in a solid matrix. Additionally, we consider that the sliding planes are rough at a finer scale; see Figure 5. The sliding plane has a saw tooth shape: It is made of alternating smooth planes of normal directions $\mathbf{n}_1$ and $\mathbf{n}_2$. In the plane formed by the normal to the plane direction ($\mathbf{n}_0$, at an angle $90^o + \theta$ from the horizontal) and the tangential direction $\mathbf{t}_0$, the plane can be represented by broken lines. The angle formed by the direction of the broken lines ($\mathbf{t}_1$ and $\mathbf{t}_2$) with the direction of the sliding plane ($\mathbf{t}_0$) is noted α. The angle α is an indicator of the roughness of the sliding plane.

The mechanism of pressure solution is explained in Figure 5B at the scale of one crack inclusion. σ_n^1 and σ_n^2 are the projections of the stress in the spherical volume on two segments of the sliding plane. Without loss of generality, we assume $\sigma_n^1 > \sigma_n^2$. The larger normal compressive stress induces a higher chemical potential at the crack surface of normal $\mathbf{n}_1$. The salt mineral thus dissolves first at the surface of normal $\mathbf{n}_1$, diffuses along the plane of normal $\mathbf{n}_1$, and finally precipitates on a surface of normal $\mathbf{n}_2$, where the chemical potential is lower. This process happens simultaneously on all the segments of normals $\mathbf{n}_1$ and $\mathbf{n}_2$ in the shear-mode crack inclusion. As a result, the initial crack surface (represented by a red solid line in Figure 5B) is transformed into another crack surface (represented with an orange dashed line). The relation between the two crack surfaces is a translation, which explains the occurrence of shear displacement along the crack plane.

3.2 | Thermodynamic model

A difference of normal stress at grain contacts triggers an increase of chemical potential μ as follows:

$$\Delta\mu = \Delta\sigma\Omega, \tag{1}$$

where Ω is the molar volume and $\Delta\sigma$ is the difference of contact normal stress on the crack surface. The chemical potential μ controls the local concentration of brine; larger chemical potentials lead to higher mineral concentrations, according to the following relation:

$$\mu = RT\ln\frac{C}{C_o}, \tag{2}$$

(A) Spherical volume with sliding plane   **(B)** Mechanism of shear displacement along a sliding plane filled with brine
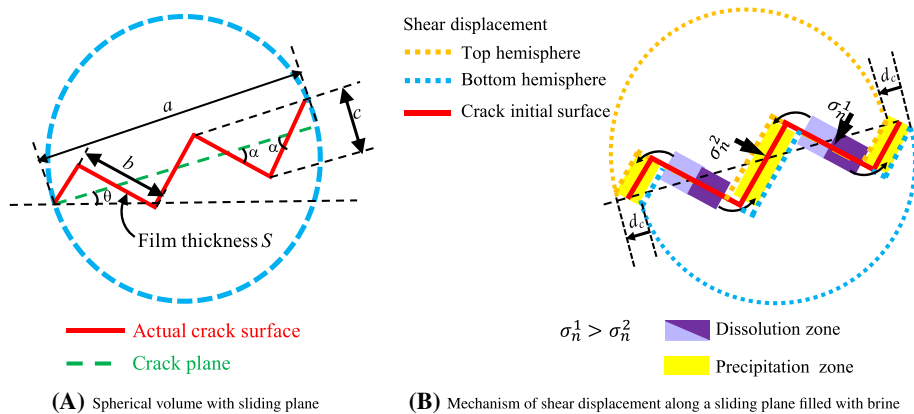
FIGURE 5   Model of a crack inclusion based on the pressure solution theory. a is the diameter of the spherical volume, b is the length of a sliding segment within the sliding plane. c represents the thickness of the rough sliding plane (of normal $\mathbf{n}_1$ and $\mathbf{n}_2$, respectively). The angle between the crack inclined segments and the crack plane is noted α.[36] σ_n^1 and σ_n^2 are the normal stresses applied on the subsurfaces of the sliding plane. d_c is the shear displacement of the spherical volume [Colour figure can be viewed at wileyonlinelibrary.com]

where R is the gas constant, T is the Kelvin temperature, C is the concentration of minerals (ions) in the fluid, and C_o is a reference concentration, which is taken equal to 6.48×10^{-6} mol/mm^3 for salt.[37] Differentiating Equation (2) with respect to C yields

$$\frac{\partial \mu}{\partial C} = \frac{RT}{C}. \tag{3}$$

According to Fick's first law, the diffusion flux $J(r)$ along a diffusion path at a location r (see Figure 6) is expressed as follows:

$$J(r) = -D\frac{\partial C}{\partial r}, \tag{4}$$

where D is the grain boundary diffusion coefficient. With the assumption that $C(r)$ can be taken as a constant C_o,[16,19,37] Equation (3) is substituted into Equation (4), which yields

$$J(r) = -D\frac{\partial C}{\partial \mu}\frac{\partial \mu}{\partial r} = -D\frac{C_o}{RT}\frac{\partial \mu}{\partial r}. \tag{5}$$

In our model, each crack inclusion is a closed thermodynamic system. Based on the mass conservation principle, the mass of mineral dissolved at grain contacts is equal to the mass of mineral that diffuses along the crack plane, which can be written as follows:

$$2dSJ(r) + \frac{2rdV_d}{\Omega} = 0, \tag{6}$$

where d is the width of the crack plane, S is the thickness of the brine film at the crack surface, and V_d is the dissolution rate of mineral at the crack surface (velocity of the dissolution front). Substituting Equations (1) and (5) into Equation (6), we have

$$\frac{\partial \sigma}{\partial r} = \frac{RTrV_d}{DC_o\Omega^2 S}. \tag{7}$$

Integrating Equation (7) along the diffusion path, the dissolution rate V_d is expressed as follows:

$$V_d = \frac{8DC_o\Omega^2 S\Delta\sigma}{RTb^2}. \tag{8}$$

According to the geometry of the cracks shown in Figure 5A, the length of a sliding segment within the sliding plane b can be expressed as follows:
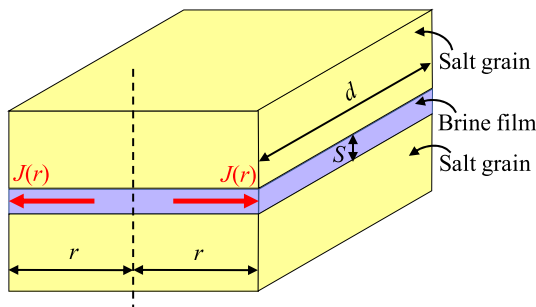

FIGURE 6 Diffusion process in the brine film. $J(r)$ is the diffusion flux at location r. d is the width of the crack plane. S is the thickness of the brine film at the crack surface [Colour figure can be viewed at wileyonlinelibrary.com]

$$c = b\sin\alpha. \tag{9}$$

As shown in Figure 5B, the tangential velocity V_c at the crack plane is related to the dissolution rate at the crack plane, as follows:

$$V_c = V_d\sin\alpha. \tag{10}$$

The shear strain rate of the crack inclusion, noted $\dot{\gamma}_c$, is induced by the tangential velocity at the crack plane and can be expressed as follows:

$$\dot{\gamma}_c = \frac{V_d\sin\alpha}{a}, \tag{11}$$

where it is reminded that we assume small deformation in the crack inclusions. Substituting Equation (8) into Equation (11) and using the geometric relationship $c = b \sin \alpha$, $\dot{\gamma}_c$ we get

$$\dot{\gamma}_c = \frac{8C_o\Omega^2}{RT}\frac{DS\sin^3\alpha\Delta\sigma}{ac^2}. \tag{12}$$

In this study, the product of the diffusion coefficient D by the thickness of the brine film S is taken as 2.0×10^{-10} mm^3/s.[37]

4 | HOMOGENIZATION SCHEME: FROM LOCAL SLIDING TO RATE-DEPENDENT REV BEHAVIOR

We formulate a 3-D homogenization scheme to upscale grain sliding mechanisms at REV scale. For this, we adopt a Mori–Tanaka scheme[26] in which each crack inclusion is a sphere that contains a sliding plane, and that is embedded in a solid matrix. That matrix is subjected to boundary conditions that are equivalent to the far field conditions imposed on the infinite medium that the crack inclusion is embedded in. According to Eshelby's theory,[22] the material properties and the stress and strain fields are uniform in the matrix and in each crack inclusion. We gather crack inclusions into families within which crack inclusions all have the same sliding plane orientation and the same sliding plane geometry (sliding plane thickness c, roughness angle α). Crack inclusions of the same family thus have the same local stress and strain fields. For the ith crack inclusion family, the local stress σ_i is expressed as a function of the local strain ϵ_i and of a local eigenstrain η_i, which adds to the eigenstrain due to stiffness heterogeneity and represents the strain field that would exist in the crack inclusion in the absence of matrix and crack inclusions around it. The microscopic stress can thus be expressed as follows[38]:

$$\sigma_i = \mathbf{C}_i : \epsilon_i - \mathbf{C}_i : \eta_i, \tag{13}$$

where $\mathbf{C}_i$ is the fourth-order stiffness tensor for the ith crack inclusion family and σ_i, ϵ_i, and η_i are all second-order tensors.

In our study, η_i is induced by the shear displacement along the sliding planes in the crack inclusions. The in-plane shear component of the second-order tensor η_i is equal to the accumulated chemical shear strain γ_c. $\dot{\gamma}_c$ can be thought of as a viscoplastic strain rate $\dot{\epsilon}^{vp}$, similar to the viscoplastic strain rate used in other models.[39-41] For example, Duvaut and Lions suggested that $\dot{\epsilon}^{vp}$ should be a function of local stress, local stiffness, and the relaxation time.[42] In Perzyna's model, $\dot{\epsilon}^{vp}$ is proportional to the derivative of yield surface with respect to local stress.[43] In our model, $\dot{\gamma}_c$ is induced by the pressure solution. Based on mass and energy principles at the inclusion scale, it is found that the chemical shear strain rate is proportional to the difference of contact normal stress on the crack surface (Equation 12). Due to strain compatibility and stress admissibility, the macroscopic strain $\bar{\epsilon}$ (respectively, the macroscopic stress $\bar{\sigma}$) is the volume average of the local strains ϵ_i (respectively, the volume average of the local stresses σ_i) in all crack inclusions over the REV. The homogenized stiffness $\mathbf{C}_{hom}$ of the REV is the volume average of the local stiffnesses, weighted by the inclusion-specific concentration tensors $\mathbf{A}_i$:

$$\mathbf{C}_{hom} = \sum_{i=0}^{n} \phi_i \mathbf{C}_i : \mathbf{A}_i, \tag{14}$$

where ϕ_i is the volume fraction of crack inclusion family i and n is the number of crack inclusion families (the index 0 refers to the matrix). The concentration tensor $\mathbf{A}_i$ is an operator that relates the local strain tensor in the ith crack inclusion family to the REV strains. Based on Eshelby's theory, the state of stress in each crack inclusion is uniform, and the concentration tensor $\mathbf{A}_i$ can be calculated as follows:[44]

$$\mathbf{A}_i = \mathbf{A}_i^\infty : \left(\sum_{j=0}^{n} \phi_i \mathbf{A}_i^\infty \right)^{-1}, \tag{15}$$

in which $\mathbf{A}_i^\infty$ is the concentration tensor that relates the local strain field in the crack inclusions of the ith family to the strain applied in the far field, $\mathbf{E}^\infty$:

$$\epsilon_i = \mathbf{A}_i^\infty : \mathbf{E}^\infty. \tag{16}$$

We have

$$\mathbf{A}_i^\infty = [\mathbf{I} + \mathbf{P}_i : (\mathbf{C}_i - \mathbf{C}_o)]^{-1}. \tag{17}$$

In the Mori–Tanaka scheme, the stiffness of the infinite medium $\mathbf{C}_o$ is equal to the matrix stiffness. $\mathbf{P}_i$ is a fourth-order tensor specific to each crack inclusion family, the expression of which can be found in the work of Mura.[45]

According to Levin's theorem,[46] the REV stress $\bar{\sigma}$ is expressed as a function of the REV strain $\bar{\epsilon}$ and of the eigenstrain of each component, as follows:

$$\bar{\sigma} = \mathbf{C}_{hom} : \bar{\epsilon} - \sum_{i=0}^{n} \phi_i \mathbf{C}_i : \eta_i : \mathbf{A}_i. \tag{18}$$

On the right side of Equation (18), the first term $(\mathbf{C}_{hom} : \bar{\epsilon})$ is the linear elasticity relation for a homogeneous medium, while the second term describes how the REV stress depends on the eigenstrain η_i (chemical viscous strain) of each component in the REV. The strain field in each phase (crack inclusion family and matrix) is related to the macroscopic strain field and to the eigenstrains of that phase, as follows:

$$\epsilon_i = \mathbf{A}_i : \bar{\epsilon} + \sum_{j=0}^{n} \mathbf{D}_{ij} \eta_j, \tag{19}$$

where $\mathbf{D}_{ij}$ is the influence tensor, which accounts for the influence of the eigenstrain of a phase on the eigenstrain of other phases. Substituting Equation (19) into Equation (13), using stress admissibility conditions and comparing with Equation (18), the expression of $\mathbf{D}_{ij}$ is found, as follows:[47]

$$\mathbf{D}_{ij} = \left\{ \delta_{ij} \mathbf{A}_i^\infty : \mathbf{P}_i - \phi_j \mathbf{A}_i : \mathbf{A}_j^\infty : \mathbf{P}_j + \left[\mathbf{A}_i : \overline{\mathbf{A}^\infty : \mathbf{P}} - \mathbf{A}_i^\infty : \mathbf{P}_i \right] : \left[\overline{(\mathbf{C}_{hom} - \mathbf{C}) : \mathbf{A}^\infty : \mathbf{P}} \right]^{-1} \right.$$
$$\left. : \phi_j \left[(\mathbf{I} - \mathbf{A}_j)^T + (\mathbf{C}_{hom} - \mathbf{C}_j) : \mathbf{A}_j^\infty : \mathbf{P}_j) \right] \right\} : \mathbf{C}_j, \tag{20}$$

where δ_{ij} and $\mathbf{I}$ are the Kronecker delta and the fourth-order identity tensor, respectively.

In the Mori–Tanaka scheme, the chemical shear strain γ_c is introduced as the eigenstrain η_i at the grain scale. The occurrence of eigenstrain triggers the redistribution of stress field and strain field in the REV (Equations 19 and 13). The updated local stress influences, in turn, the evolution of eigenstrain (chemical viscous strain) at the grain scale (Equation 12).

5 | MODEL CALIBRATION

The proposed Mori–Tanaka homogenization model is now calibrated against the results presented in Section 2 for the sets of small loading cycles performed at 0% and 3.8% permanent strain. The distribution of the orientation of the sliding planes was obtained by image analysis (Figure 7). Tens of optical petrographic images were stitched together to allow observation of 1–200 grains. Grain boundaries were manually traced, and opening-mode microcracks were identified based on two criteria: (1) There is a clear separation between two salt grain boundaries; and (2) the opposing sides of these two salt grain boundaries match well geometrically, which indicates that they were previously in contact. Since sliding on a flaw cannot produce a displacement without opening a crack at the tip of the flaw, we assumed that opening-mode cracks indicated the propagation of shear-mode cracks. Accordingly, we assumed that a grain boundary that slides is a grain boundary that (Figure 8)

- Either connects to an intergranular opening-mode crack at one end and to a void at the other end;
- Or connects to an intergranular opening-mode crack at each of its ends.

We counted the number of sliding planes (N_s) and the number of boundary sections (N_b) in the microscopic images, which allowed us to calculate the following 2-D sliding plane density φ, as follows:

$$\varphi = \frac{N_s}{N_b}. \tag{21}$$

The mechanical properties of the crack inclusions were then calibrated against the stress–strain curves obtained experimentally, as described below.

We introduce the following relationship between the sliding plane density φ and the volume fraction of the crack inclusions (ϕ_c) considered in the REV:

$$\phi_c = \beta_1 \varphi^{\beta_2}, \tag{22}$$

where β_1 and β_2 are parameters that need to be calibrated. For simplicity, we assume that all crack inclusion orientations are represented with the same volume fraction ϕ_c/N_s.

The orientation angle of a crack plane obtained by image analysis in 2D is taken equal to the angle formed by the crack plane with the horizontal in 3D, which is identical to the angle between the normal direction of the crack plane
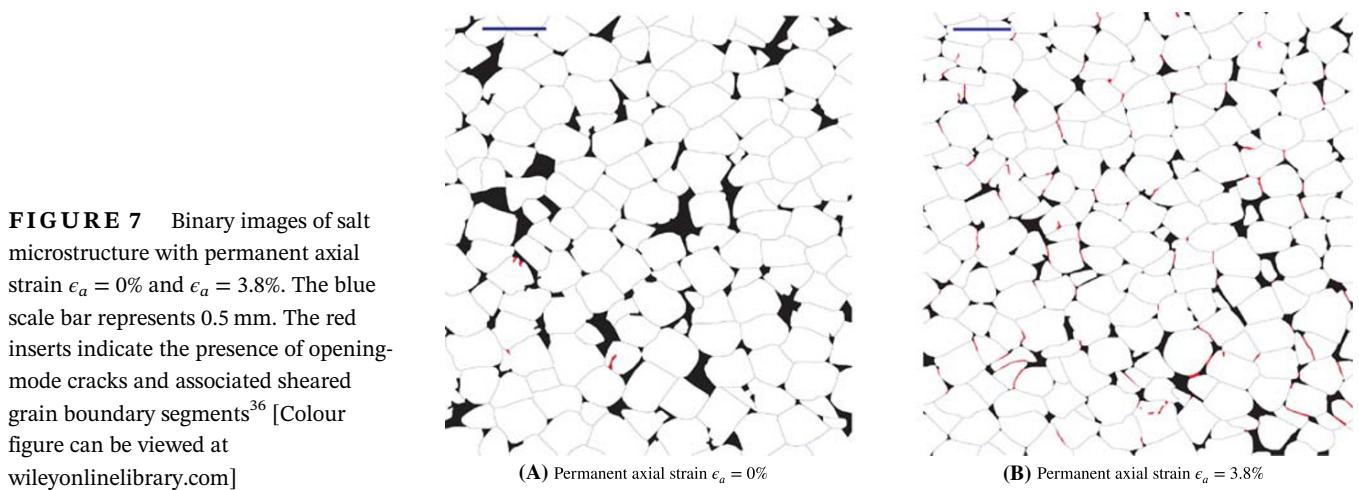
FIGURE 7 Binary images of salt microstructure with permanent axial strain $\epsilon_a = 0\%$ and $\epsilon_a = 3.8\%$. The blue scale bar represents 0.5 mm. The red inserts indicate the presence of opening-mode cracks and associated sheared grain boundary segments[36] [Colour figure can be viewed at wileyonlinelibrary.com]

(A) Permanent axial strain $\epsilon_a = 0\%$

(B) Permanent axial strain $\epsilon_a = 3.8\%$

FIGURE 8 Schematic showing the interpretation of the microscopic images to find the sliding cracks. Blue arrows show the shearing directions [Colour figure can be viewed at wileyonlinelibrary.com]

Sliding cracks
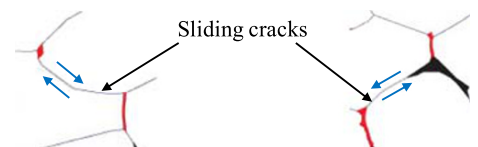
and the loading axis, that is, θ in Figures 5 and 9. We assume that the angle of revolution of the crack planes around the loading axis (often noted ψ) is uniformly distributed in the REV. This hypothesis is supported by the fact that (i) specimens were fabricated by consolidating salt aggregates at high temperature and where statistically identical to one another; (ii) the loading conditions and the shape of the specimen were axis-symmetric. We sorted the values of θ obtained by image analysis for all the sliding planes, by ascending order. We divided the interval of variation of the angle θ into 10 subintervals. In each subinterval, the mean of θ was calculated. The distribution of θ in the REV was defined by the 10 mean θ values, weighted by the number of occurrences of θ in that interval, and normalized by the total number of angles θ observed in the image. Ten uniformly distributed values of ψ, ranging from 0° to 360°, were used to define the distribution of the revolution angles of the crack inclusions of the REV. As a result, 100 crack inclusion families were defined, each having a specific orientation defined by a couple of angles (θ, ψ).

By analogy with damage mechanics, we introduce two parameters C_K and C_G to account for the stiffness degradation of the crack inclusions as a consequence of sliding (similar to the evolution of microscopic cracks). C_K and C_G range from 0 to 1.[48] The bulk modulus K_i and the shear modulus G_i of the crack inclusions of family i are calculated as follows:

$$K_i = C_K K_m, \tag{23}$$

$$G_i = C_G G_m, \tag{24}$$

where K_m and G_m are bulk and shear moduli of the matrix, respectively.

In the small compression cycles done with a permanent axial strain equal to 0%, few sliding planes are observed. The stiffness of the salt rock REV is controlled by the stiffness of the matrix. We thus calibrate the bulk and shear moduli of the matrix (K_m and G_m) against the results of the small cyclic compression cycles with a zero permanent strain. In the small compression cycles done with a permanent axial strain equal to 3.8%, very small chemical shear strain occurs in the first cycle C1, because the strain rate is high, and the period of time of the loading is small. The deformation of salt rock in C1 is controlled by the modulus reduction parameters C_K and C_G, and the volume fraction of the crack inclusions, ϕ_c. ϕ_c depends on the parameters β_1 and β_2 (Equation 22). So the parameters β_1, β_2, C_K, and C_G are fitted to match the stress–strain curve C1. The geometry of the crack planes and the volume fraction of the crack inclusion families influence the reduction of stiffness and the development of hysteresis in the three cycles C1, C2, and C3. The parameters controlling the geometry of the crack planes are the roughness angle α and the thickness of the crack plane, c. We calibrate α and c to match the stress–strain curves in C2 and C3. We did not simulate the deformation of salt rock during the waiting period of time between small loading cycles, which resulted in a loss of accuracy. Cycles C2 and C3 were manually shifted and initialized at the same initial axial strain as that recorded in the experiments. The calibrated parameters are listed in Table 1, and simulations done at the material point with the calibrated model are shown in Figures 10 and 11. The typical shear modulus of salt rock ranges from 8.85 to 15.60 GPa, and the typical bulk modulus
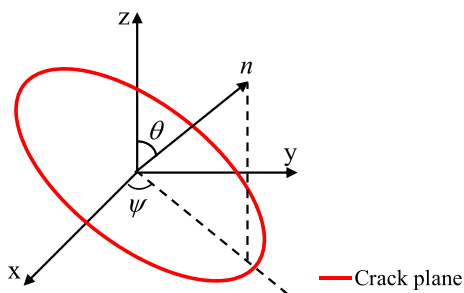

FIGURE 9 The orientation of a crack plane. The z axis is the loading direction. θ is the angle between normal direction (n) of a crack plane and the z axis. ψ represents the angle between the x axis and the projection of the normal direction of the crack plane on the horizontal plane (xy plane). [Colour figure can be viewed at wileyonlinelibrary.com]

TABLE 1 Parameters of the rate-dependent micro–macro model of salt calibrated against the results of the small loading cycles at 0% and 3.8% permanent axial strain

Mechanical properties						Crack geometry	
K_m	G_m	C_K	C_G	β_1	β_2	c	α
GPa	GPa	–	–	–	–	μm	^{o}
17.0	10.5	0.9	0.6	1.91	1.34	2.0	30

FIGURE 10 Model calibration against the results of the small loading cycles at a permanent axial strain $\epsilon_a = 0\%$. Solid lines: simulation results. Dashed lines: experimental results [Colour figure can be viewed at wileyonlinelibrary.com]
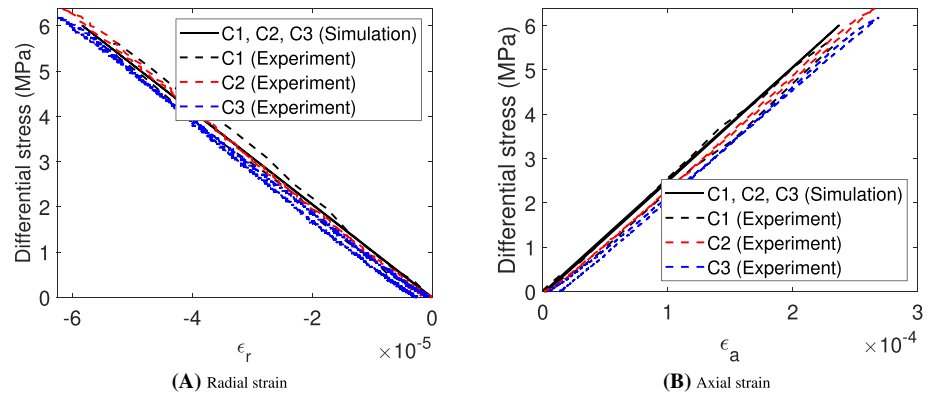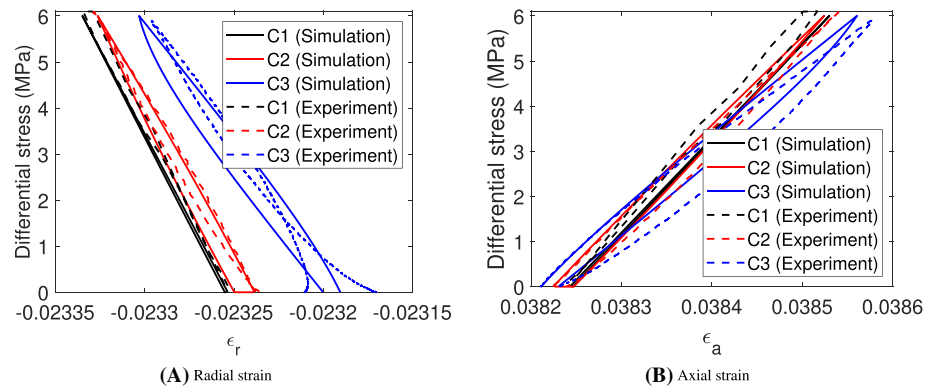

(A) Radial strain

(B) Axial strain

FIGURE 11 Model calibration against the results of the small loading cycles at a permanent axial strain $\epsilon_a = 3.8\%$. Solid lines: simulation results. Dashed lines: experimental results [Colour figure can be viewed at wileyonlinelibrary.com]

(A) Radial strain

(B) Axial strain

of salt rock ranges from 14.89 to 42.5 GPa.[11,49,50] The calibrated bulk and shear moduli fall in these ranges. Due to the low confinement, the values of the moduli are relatively small.

When the permanent axial strain ϵ_a is 0%, no sliding planes develop. Brine is isolated in the fluid inclusions, and there is no brine film at the grain boundaries to facilitate the pressure solution process. The simulation results show that the stress–strain curves obtained for the small loading cycles C1, C2, and C3, conducted at different strain rates, are superimposed, which indicates that the effects of chemical reactions are negligible (Figure 10). According to Figure 11, our model can well capture the stiffness reduction and hysteresis evolution of salt rock, which are observed at a permanent strain of 3.8%.

Figure 12A presents the development of local normal contact stress on the segments n_1 and n_2 of a crack surface in one of the crack inclusion families, during the small loading cycles performed at a permanent axial strain of 3.8 %. Initially, during C1, the compressive normal stress on segment n_1 (σ_n^1) is much larger than the compressive normal stress on segment n_2 (σ_n^2). Then, the difference between σ_n^1 and σ_n^2 decreases. During the unloading phase of C2, σ_n^1 gets equal to σ_n^2 (intersection of the red dashed line and the red solid line in Figure 12A). Then, the chemical shear strain γ_c starts to decrease as shown in Figure 12B. The strain rate in C3 is 1/10 of the strain rate of C2, and the duration of C3 is 10 times that of C2. γ_c is 2.0×10^{-4} when $\Delta\epsilon_a$ reaches its maximum value in C3, which is only four times the value of γ_c when $\Delta\epsilon_a$ reaches its maximum in C2 (0.5×10^{-4}). This is because the smaller difference between σ_n^1 and σ_n^2 decelerates the accumulation of chemical strain (Equation 12).

6 | SENSITIVITY ANALYSIS

We now investigate the sensitivity of the deformation of the REV to the geometry of the crack plane (thickness of crack c and roughness angle α) and to the volume fraction of the crack inclusion families. In all the simulations presented in the following, the angle between the direction of the crack planes and the horizontal direction is set equal to 60°. The strain rate is 3×10^{-6}/s. The mechanical properties calibrated above are adopted (see Table 1). In this section, we compare the model predictions for crack thicknesses of 1, 3, 5, and 7 μm[51] and for roughness angles of 10°, 30°, 45°, and 60°.[52]
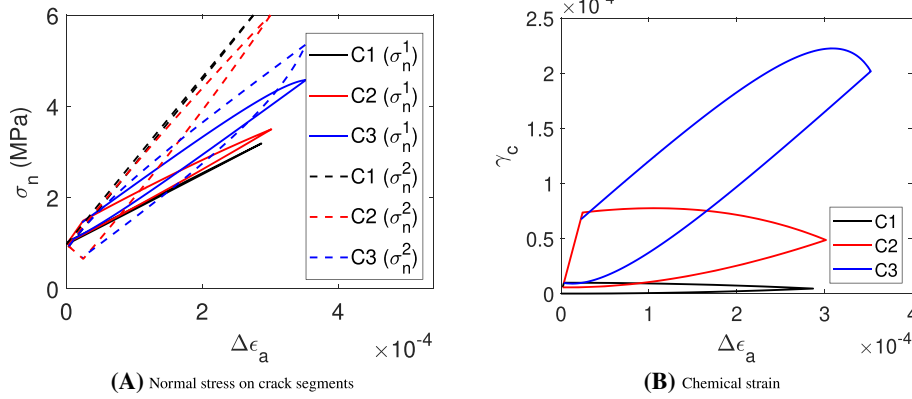
FIGURE 12 Local normal stress and chemical strain in a representative crack inclusion family in which the orientation of the crack plane is 25°. The difference of normal stress between the planes of normal n_1 and n_2 decreases during the unloading phases. The chemical strain starts decreasing when the sign of the difference of normal stress is altered [Colour figure can be viewed at wileyonlinelibrary.com]
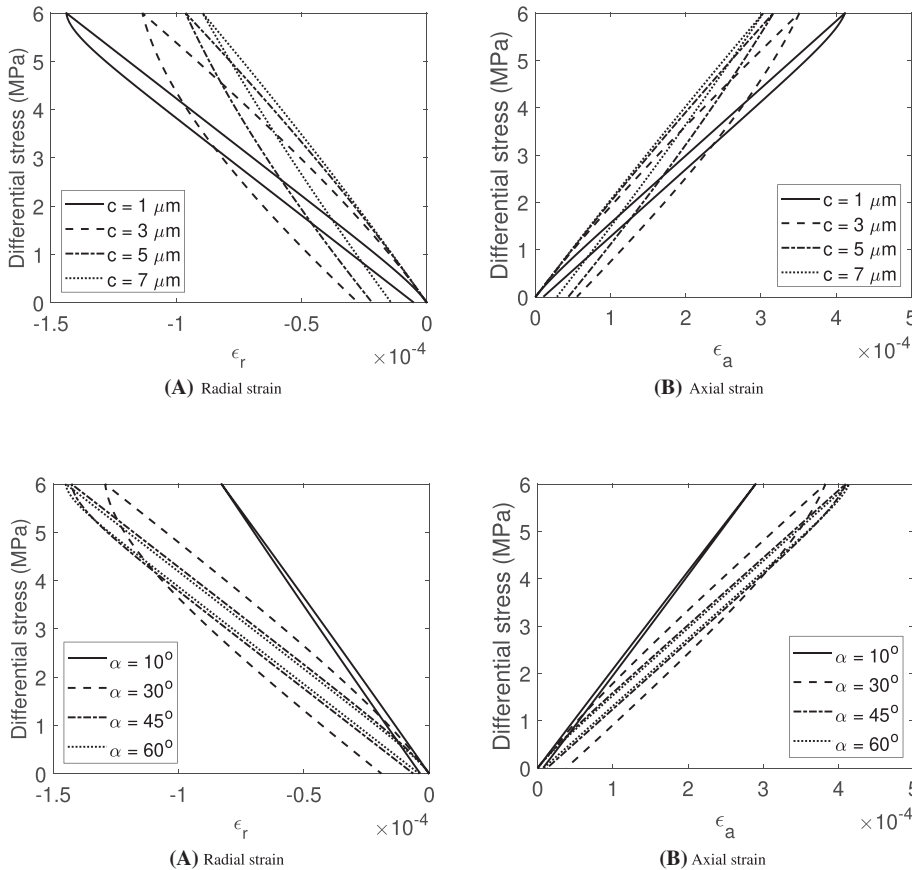
(A) Normal stress on crack segments

(B) Chemical strain

FIGURE 13 Influence of crack thickness on the stress–strain relationship. The total volume fraction of the crack inclusions, ϕ_c, is equal to 50%. The roughness angle α is set equal to 30°. More irreversible deformation accumulates for very large or very small crack thicknesses. The hysteresis is less pronounced when the crack film is either very thin or thick
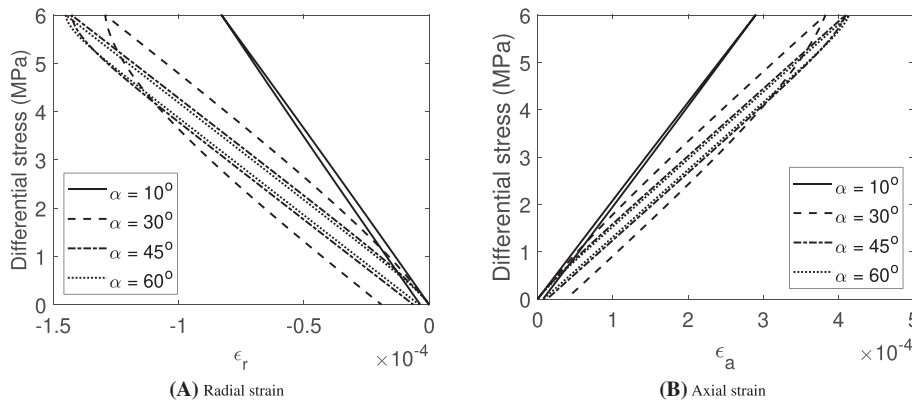
(A) Radial strain

(B) Axial strain

FIGURE 14 Influence of the roughness angle α on the stress–strain relationship. The total volume fraction of crack inclusions, ϕ_c, is equal to 50%. The crack thickness c is set equal to $2.0\,\mu$m. A larger angle α enhances the accumulation of irreversible deformation and the development of hysteresis

(A) Radial strain

(B) Axial strain

According to Figure 13, larger chemical strain and larger deformation are produced for thinner cracks, which is consistent with Equation (12). A thinner sliding plane provides a shorter diffusion path from the crack plane segment with large normal stress to the crack plane segment with small normal stress. More salt mineral is dissolved at the grain contacts, and the shear displacement increases. When c is very small (i.e., $c = 1\,\mu$m), the stress of the crack inclusions is redistributed very rapidly because the dissolution rate is very high at grain contacts. As a result, chemical strain develops in the direction opposite to the sliding, and hysteresis reduces.

Figure 14 shows that a larger roughness angle α enhances the accumulation of irreversible deformation and the development of hysteresis. When α is larger than 45°, the influence of α becomes insignificant. A larger roughness angle α decreases the length of the diffusion path of salt ions, which enhances the shear strain of the crack inclusions. In addition, the roughness angle α controls the difference in normal stress, $\sigma_n^1 - \sigma_n^2$. When α is very small, segments n_1 and segments n_2 have very similar orientations (Figure 5A). Hence, the difference of normal stress becomes negligible, and as a result, the shear strain rate of the crack inclusion is very small.

The volume fraction of the crack inclusions (ϕ_c) does not influence the local chemical shear strain rate in the crack inclusions. However, a larger ϕ_c amplifies the effect of local strains on the macroscopic deformation of the REV, including the elastic strain (Equation 14) and the chemical strain induced by pressure solution (Equation 18). The larger the volume fraction ϕ_c, the larger the REV deformation and the larger the hysteresis, as shown in Figure 15.

7 | ENERGY DISSIPATION

The hysteresis and the residual strain observed in the tests indicate that energy is dissipated during the loading and unloading cycles. Figure 16A presents the external work input to the salt rock REV for different values of the crack thickness (c), for a strain rate is 3×10^{-6}/s. The roughness angle α is set equal to 30°, and the total volume fraction of the crack inclusions, ϕ_c, is equal to 50%. In each cycle, the specimen is unloaded after the maximum differential stress reaches 6 MPa. Therefore, the maximum external work ever provided to the REV can be calculated by multiplying the maximum axial strain by 6 MPa.

As can be seen from Figure 16, a smaller crack thickness is accompanied by a faster pressure solution process at the crack faces, which enhances the local chemical strain and increases the maximum strain undergone by the REV. As a result, the smaller the crack thickness, the larger the maximum external work at the REV scale. When c is large ($c > 7\,\mu$m), the rate of pressure solution is too small to influence the chemical strain or trigger any hysteresis. When c is small ($c < 1\,\mu$m), pressure solution happens so quickly that stress is redistributed quasi-instantaneously in the salt REV during the loading path. The maximum strain of the REV is not influenced by pressure solution. Little energy is dissipated during the loading cycle when c is large or small, because hysteresis is negligible.

Figure 17 shows that the volume fraction of the crack inclusions largely influences the external work provided to the salt rock REV. In these simulations, the roughness angle α was set equal to 30°. The crack thickness c was set equal to $2.0\,\mu$m. Figure 17A suggests that a higher volume fraction of crack inclusions amplifies the effects of the chemical strains in the crack inclusions, which yields more chemical strain and irreversible deformation at the REV scale. As a result, both the maximum external work and the dissipated energy increase with the volume fraction of the crack inclusions.

FIGURE 15 Influence of the volume fraction of the crack inclusions on the stress–strain relationship. The roughness angle α is set equal to 30°. The crack thickness c is set equal to $2.0\,\mu$m. Irreversible deformation and hysteresis increase with the volume fraction of the crack inclusions in the REV
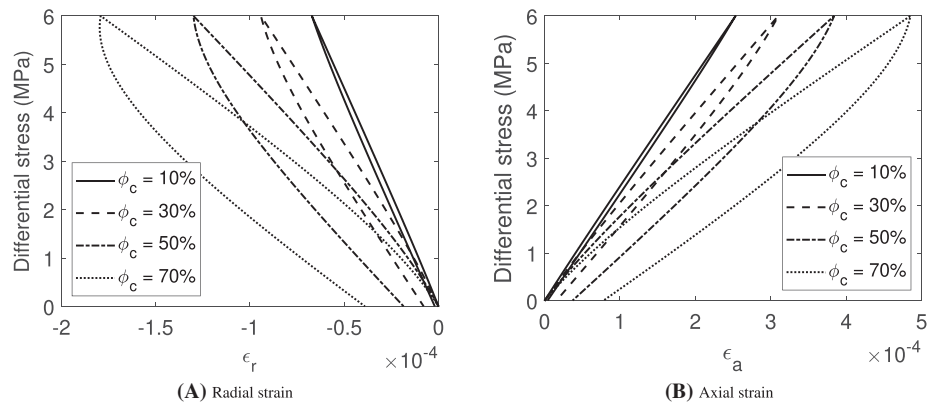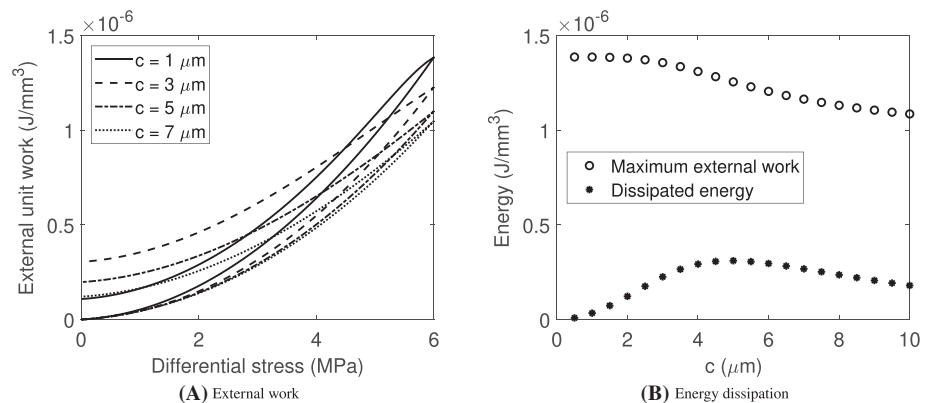

(A) Radial strain   **(B)** Axial strain

FIGURE 16 Influence of crack thickness on energy dissipation. The roughness angle α is set equal to 30°. The total volume fraction of the crack inclusions, ϕ_c, is equal to 50%. A smaller crack thickness induces a larger maximum external unit work. The energy dissipated by diffusion is negligible when the thickness of cracks is either very larger or very small
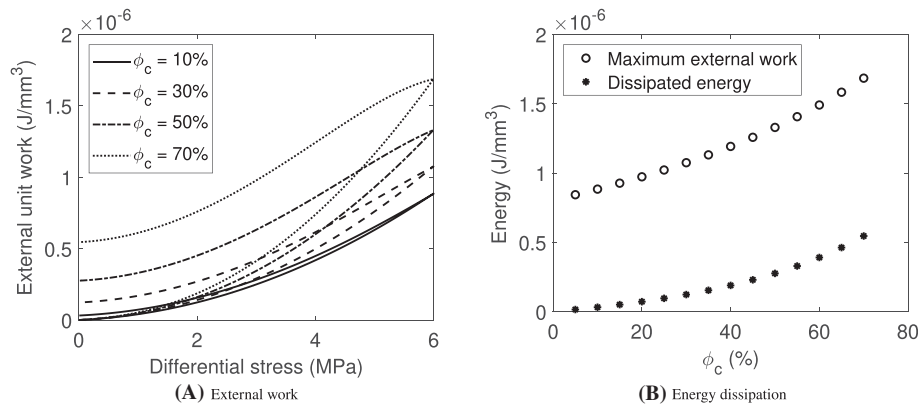

(A) External work   **(B)** Energy dissipation

FIGURE 17 Influence of the volume fraction of the crack inclusions on energy dissipation. The roughness angle α is set equal to 30°. The crack thickness c is set equal to $2.0\,\mu$m. A larger volume fraction of crack inclusions leads to greater external work applied to the salt rock REV and to more energy dissipated by pressure solution

To summarize, pressure solution can induce significant hysteresis, which may reduce the efficiency of geological storage facilities that are loaded cyclically, such as CAES caverns. From the analysis above, we conclude that CAES is most efficient in undamaged salt rock with only a few sliding planes or in salt rock where the pressure solution rate is either very large (small crack thickness c) or very small (large crack thickness c).

8 | CONCLUSIONS

A chemo-mechanical homogenization framework is proposed to capture the rate-dependent behavior of salt rock during cyclic compression loading. The REV is viewed as a homogeneous matrix that contains sliding cracks. A crack inclusion is defined as a spherical volume around a sliding crack that has rough surfaces. Field variables at the REV scale are calculated as the average of the local field variables over all the possible distributions of orientation, crack thickness and roughness angle of the crack inclusions. The shear displacement of the sliding planes is related to the mass of salt ions that diffuse along the crack surface. The rate of diffusion is calculated by a pressure solution model. The shear deformation of a crack inclusion due to pressure solution defines the chemical eigenstrain of that crack inclusion. The relationship between the inclusion-scale stresses and strains and the REV scale stresses and strains is established by using the Mori–Tanaka homogenization scheme.

The proposed rate-dependent homogenization model is calibrated against cyclic compression tests. It is noted that a lower strain rate and/or a larger number of sliding cracks enhances stiffness reduction and hysteresis. Sensitivity analyses show that thinner sliding cracks (i.e., thinner brine films) promote stiffness reduction and accelerate stress redistributions in the crack inclusions. Higher roughness angles lead to an increased difference of normal stress along the different segments of the crack plane and to a reduced diffusion path, which both amplify the reduction of stiffness and the development of hysteresis. The larger the volume fraction of the crack inclusions, the larger the REV deformation and the larger the hysteresis—this is because the presence of a higher number of sliding planes amplifies the effects of the local shear strains driven by pressure solution. In the proposed framework, we simplified the model by assuming same thickness for all cracks and same roughness angle for each component in the REV. Assuming homogeneous crack thickness and roughness angle leads to delayed stress redistribution under the proposed homogenization framework, hence to larger REV deformation. These limitations could be overcome by lifting some of the restricting geometrical assumptions, provided that experimental data can support model calibration.

Our results confirm that the rate-dependent behavior of salt rock is governed by pressure solution on grain boundaries at low pressure and low temperature. The proposed model provides the first micromechanical explanation of the rate dependent behavior of salt under cyclic loading at room temperature. The homogenization scheme can easily be adapted to other geomaterials that are subject to pressure solution or chemical weathering. Results presented in this study shed light on the design of geological storage facilities that undergo cyclic unloading, which could help optimize the energy production cycle with low carbon emissions.

List of symbols

a radius of crack inclusions
$\mathbf{A}_i$ concentration tensor of the component i
$\mathbf{A}_i^o$ concentration tensor of the matrix component
α angle between the plane of sliding plane and its subsurfaces
b length of the subsurface of sliding planes
β volume fraction parameter
c thickness of shear-mode cracks
C concentration of minerals (ions) in the fluid
C_o reference concentration
C_K, C_G parameters for bulk and shear moduli degradation
$\mathbf{C}_{hom}$ homogenized stiffness of the REV
$\mathbf{C}_i$ stiffness of the component i
$\mathbf{C}_o$ stiffness of matrix
γ_c shear strain of the crack inclusion
$\mathbf{D}_{ij}$ influence tensor
d width of the subsurface of shear-mode cracks
D grain boundary diffusion coefficient
δ_{ij} Kronecker delta
ϵ_i local total strain of component i
ϵ_m strain field in the matrix
ϵ_v volumetric strain of the REV
$\bar{\epsilon}$ strain of the REV
ϕ_i volume fraction of component i
G shear modulus
η eigenstrain of crack inclusions
$\mathbf{I}$ fourth-order identity tensor
J diffusion flux along subsurface
K bulk modulus
n number of components in the REV
N_s number sliding planes counted in the microscopic images
N_b number of boundary sections counted in the microscopic images
$\mathbf{n}$ the normal direction of crack plane
θ orientation of the sliding plane plane from the horizontal
R gas constant
S thickness of the brine film at the crack surface
σ_i local total stress of component i
σ_n normal stress applied on the subsurface of shear-mode cracks
$\bar{\sigma}$ stress of the REV
$\mathbf{t}$ the tangential direction of crack plane
T Kelvin temperature
ϕ_c volume fraction of all the crack inclusions
φ density of sliding planes
V_d dissolution rate at the subsurface
V_c tangential velocity at the crack plane
ψ angle of revolution of the crack planes around the loading axis
Ω molar volume of NaCl

ORCID

Xianda Shen 🔾 https://orcid.org/0000-0001-8321-9910

REFERENCES

1. Knipe RJ. Deformation mechanisms—recognition from natural tectonites. *J Struct Geol*. 1989;11(1-2):127–146.
2. Fredrich JT, Evans B, Wong T-F. Micromechanics of the brittle to plastic transition in carrara marble. *J Geophys Res Solid Earth*. 1989;94(B4):4129–4145.
3. Paterson MS, Wong T-f. *Experimental Rock Deformation-the Brittle Field*. Berlin, Heidelberg: Springer Science & Business Media; 2005.
4. Chester FM. Dynamic recrystallization in semi-brittle faults. *J Struct Geol*. 1989;11(7):847–858.
5. Ghahremani F. Effect of grain boundary sliding on anelasticity of polycrystals. *Int J Solids Struct*. 1980;16(9):825–845.
6. Zener C. Theory of the elasticity of polycrystals with viscous grain boundaries. *Phys Rev*. 1941;60(12):906.
7. Chester FM. The brittle-ductile transition in a deformation-mechanism map for halite. *Tectonophysics*. 1988;154(1-2):125–136.
8. Raj R, Ashby MF. On grain boundary sliding and diffusional creep. *Metall Trans*. 1971;2(4):1113–1127.
9. Urai JL, Spiers CJ, Zwart HJ, Lister GS. Weakening of rock salt by water during long-term creep. *Nature*. 1986;324(6097):554–557.
10. Lajtai EZ, Duncan EJS, Carter BJ. The effect of strain rate on rock strength. *Rock Mech Rock Eng*. 1991;24(2):99–109.
11. Senseny PE, Hansen FD, Russell JE, Carter NL, Handin JW. Mechanical behaviour of rock salt: phenomenology and micromechanisms. *Int J Rock Mech Min Sci Geomech Abstr*. 1992;29(4):363–378.
12. Fuenkajorn K, Sriapai T, Samsri P. Effects of loading rate on strength and deformability of maha sarakham salt. *Eng Geol*. 2012;135:10–23.
13. Wheeler J. Anisotropic rheology during grain boundary diffusion creep and its relation to grain rotation, grain boundary sliding and superplasticity. *Philos Mag*. 2010;90(21):2841–2864.
14. McClay KR. Pressure solution and coble creep in rocks and minerals: a review. *Geol Soc Spec Publ*. 1977;134(1):57–70.
15. Paterson MS. Nonhydrostatic thermodynamics and its geologic applications. *Rev Geophys*. 1973;11(2):355–389. https://doi.org/10.1029/RG011i002p00355
16. Rutter EH, Elliott D. The kinetics of rock deformation by pressure solution. *Philos Trans R Soc A*. 1976;283(1312):203–219.
17. Raj R. Creep in polycrystalline aggregates by matter transport through a liquid phase. *J Geophys Res Solid Earth*. 1982;87(B6):4731–4739. https://doi.org/10.1029/JB087iB06p04731
18. Rutter EH. Pressure solution in nature, theory and experiment. *Geol Soc Spec Publ*. 1983;140(5):725–740.
19. Lehner FK. A model for intergranular pressure solution in open systems. *Tectonophysics*. 1995;245(3-4):153–170.
20. Drugan WJ, Willis JR. A micromechanics-based nonlocal constitutive equation and estimates of representative volume element size for elastic composites. *J Mech Phys Solids*. 1996;44(4):497–524.
21. Gross D, Seelig T. *Fracture Mechanics: With an Introduction to Micromechanics*. Berlin: Springer; 2017.
22. Eshelby JD. The determination of the elastic field of an ellipsoidal inclusion, and related problems. *P Roy Soc Lon A-Math Phy Eng Sci*. 1957;241(1226):376–396.
23. Vieville P, Bonnet AS, Lipiński P. Modelling effective properties of composite materials using the inclusion concept. General considerations. *Arch Appl Mech*. 2006;58(3):207–239.
24. Lurie S, Solyaev Y, Shramko K. Comparison between the Mori–Tanaka and generalized self-consistent methods in the framework of anti-plane strain inclusion problem in strain gradient elasticity. *Mech Mater*. 2018;122:133–144.
25. Shen X, Arson C. An isotropic self-consistent homogenization scheme for chemo-mechanical healing driven by pressure solution in halite. *Int J Solids Struct*. 2019;161:96–110.
26. Mori T, Tanaka K. Average stress in matrix and average elastic energy of materials with misfitting inclusions. *Acta Mater*. 1973;21(5):571–574.
27. Benveniste Y. A new approach to the application of Mori–Tanaka's theory in composite materials. *Mech Mater*. 1987;6(2):147–157.
28. Ma H, Hu G, Huang Z. A micromechanical method for particulate composites with finite particle concentration. *Mech Mater*. 2004;36(4):359–368.
29. Kim J, Lee J-K. A new model to predict effective elastic constants of composites with spherical fillers. *J Mech Sci Technol*. 2006;20(11):1891–1897.
30. Tucker CL III, Liang E. Stiffness predictions for unidirectional short-fiber composites: review and evaluation. *Compos Sci Technol*. 1999;59(5):655–671.
31. Pichler B, Dormieux L. Cracking risk of partially saturated porous media—part i: microporoelasticity model. *Int J Numer Anal Met*. 2010;34(2):135–157.
32. Lu P. Further studies on mori–tanaka models for thermal expansion coefficients of composites. *Polymer*. 2013;54(6):1691–1699.
33. Castañeda PP, Willis JR. The effect of spatial distribution on the effective behavior of composite materials and cracked media. *J Mech Phys Solids*. 1995;43(12):1919–1951.
34. Ding J. Grain boundary processes, anelasticity, and test of the effective stress law for semibrittle deformation of synthetic salt-rocks. *Ph. D. Thesis*; 2019.
35. Shen X, Arson C, Ding J, Chester FM, Chester JS. Mechanisms of anisotropy in salt rock upon microcrack propagation. *Rock Mechanics and Rock Engineering*. 2020;53:3185–3205.
36. Ding J, Chester FM, Chester JS, Xianda S, Arson C. Microcrack network development in salt-rock during cyclic loading at low confining pressure. In *51st US Rock Mechanics/Geomechanics Symposium of the American Rock Mechanics Association*. San Francisco, CA.; 2017.
37. Schutjens PMTM, Spiers CJ. Intergranular pressure solution in nacl: grain-to-grain contact experiments under the optical microscope. *Oil Gas Sci Technol*. 1999;54(6):729–750.

38. Pichler B, Hellmich C. Estimation of influence tensors for eigenstressed multiphase elastic media with nonaligned inclusion phases of arbitrary ellipsoidal shape. *J Eng Mech*. 2010;136(8):1043–1053.

39. Borja RI, Yin Q, Zhao Y. Cam-clay plasticity. part ix: on the anisotropy, heterogeneity, and viscoplasticity of shale. *Comput Method Appl M Eng*. 2020;360:112695.

40. Firme PedroALP, Brandao NB, Roehl D, Romanel C. Enhanced double-mechanism creep laws for salt rocks. *Acta Geotech*. 2018;13(6): 1329–1340.

41. Zhang N, Nagel T. Error-controlled implicit time integration of elasto-visco-plastic constitutive models for rock salt. *Int J Numer Anal Met*. 2020;44(8):1109–1127.

42. Duvant G, Lions JL. *Inequalities in Mechanics and Physics*. Vol 219. Berlin, Germany: Springer Science & Business Media; 1976.

43. Perzyna P. Fundamental problems in viscoplasticity. *Adv Appl Mech*. 1966;9:243–377.

44. Hill R. Continuum micro-mechanics of elastoplastic polycrystals. *J Mech Phys Solids*. 1965;13(2):89–101.

45. Mura T. *Micromechanics of Defects in Solids*. Dordrecht: Springer Science & Business Media; 2013.

46. Levin VM. Thermal expansion coefficient of heterogeneous materials. *Mekhanika Tverdogo Tela*. 1967;2(1):83–94.

47. Shen X, Arson C, Ferrier KL, West N, Dai S. Mineral weathering and bedrock weakening: modeling microscale bedrock damage under biotite weathering. *J Geophys Res Earth Surf*. 2019;124(11):2623–2646.

48. Lemaitre J. A Continuous Damage Mechanics Model for Ductile Fracture. *J Eng Mater Tech*. 1985;107(1):83–89. https://doi.org/10.1115/1.3225775

49. Pouya A, Zhu C, Arson C. Micro–macro approach of salt viscous fatigue under cyclic loading. *Mech Mater*. 2016;93:13–31.

50. Fuenkajorn K, Phueakphum D. Effects of cyclic loading on mechanical properties of maha sarakham salt. *Eng Geol*. 2010;112(1-4): 43–52.

51. Liu Y, Ning L, Ecke RE. Dynamics of surface patterning in salt-crystal dissolution. *Phys Rev E*. 1996;53(6):R5572.

52. Desbois G, Urai JL, Kukla PA, et al. Distribution of brine in grain boundaries during static recrystallization in wet, synthetic halite: insight from broad ion beam sectioning and sem observation at cryogenic temperature. *Contrib Mineral Petrol*. 2012;163(1):19–31.